Supporting Information: Blocking Lithium Dendrite Growth in Solid-State Batteries with an Ultrathin Amorphous Li-La-Zr-O Solid Electrolyte.

Jordi Sastre,*,† Moritz H. Futscher,† Lea Pompizi,† Abdessalem Aribia,† Agnieszka Priebe,‡ Jan Overbeck,¶ Michael Stiefel,¶ Ayodhya N. Tiwari,† and Yaroslav E. Romanyuk†

†*Laboratory for Thin Films and Photovoltaics, Empa - Swiss Federal Laboratories for Materials Science and Technology, Überlandstrasse 129, CH-8600 Dübendorf, Switzerland*

‡*Laboratory for Mechanics of Materials and Nanostructure, Empa - Swiss Federal Laboratories for Materials Science and Technology, Feuerwerkerstrasse 39, CH-3602 Thun, Switzerland*

¶*Transport at Nanoscale Interfaces, Empa - Swiss Federal Laboratories for Materials Science and Technology, Überlandstrasse 129, CH-8600 Dübendorf, Switzerland*

E-mail: jordi.sastrepellicer@empa.ch

Phone: +41 58 765 61 10

1 Sample preparation

1.1 Amorphous Li-La-Zr-O sputtering deposition

Amorphous Li-La-Zr-O (aLLZO) films were deposited at room temperature in a radio-frequency (RF) magnetron sputtering system (Orion, AJA International Inc.) with a confocal off-axis target configuration. A $Li_{6.25}Ga_{0.25}La_3Zr_2O_{12}$ target was co-sputtered simultaneously with a Li_2O target (Toshima Manufacturing Co.) in order to overlithiate the films. The sputtering process was performed at 0.30 Pa using a gas flow of 50 sccm Ar and 1 sccm Ar:O_2. The deposition rate of each target was controlled independently via the sputtering power and monitored using a quartz crystal microbalance (QCM) sensor. The deposition time was adjusted to obtain films with thicknesses in the range of 50 to 100 nm with typical times not exceeding 1 hour. Optimized films were prepared with a sputtering power of 1.50 W cm^{-2} on the LLZO target and 7.60 W cm^{-2} on the Li_2O target and had a thickness of 70 nm. As a reference for crystalline LLZO, films prepared as previously shown by our group were used.[S1]

1.2 Substrates and metal electrodes

Different types of substrates were employed for the different characterization techniques. XRD, Raman and FT-IR measurements were carried out on aLLZO films deposited on (100)-oriented single-crystal MgO substrates (Jiangyin Maideli Advanced Materials Co.,Ltd.). Impedance spectroscopy and transient electrical measurements were carried out on aLLZO films deposited on Pt-coated Si substrates. Single-side polished (100) Si wafers (University Wafer) were first coated with a 60 nm MgO film to improve adhesion and block Li-ion migration into the Si wafer. MgO was deposited from a a MgO target (Stanford Advanced Materials) in a CT200 magnetron sputtering cluster tool (Alliance Concept). The sputtering was carried out with a power of 3.10 W cm^{-2}, a gas flow of 60 sccm Ar + 0.5 sccm O_2, and a chamber pressure of 0.60 Pa. The wafers were later annealed at 850 °C for 3 h in air. As

back electrode, a 20 nm Ti adhesion layer followed by 300 nm Pt layer were deposited by RF magnetron sputtering in an Orion sputtering system. The Ti and Pt targets (Plasmaterials Inc.) were sputtered with power of $3\,\mathrm{W\,cm^{-2}}$ with a 50 sccm Ar flow and a pressure of 0.30 Pa. After depositing the aLLZO films, 50 nm Au contacts with a diameter of 1 mm were deposited on top by thermal evaporation (Nexdep, Angstrom Engineering Inc.) from Au pellets (Kurt J. Lesker Company) with a rate of about $1\,\mathrm{Å\,s^{-1}}$ at a pressure of about 1×10^{-4} Pa. For the Li/Pt half-cell measurements, the same type of Pt-coated sapphire substrate was employed and an aLLZO film with about double the standard thickness was deposited on top. On top of the aLLZO film, 5 µm metallic Li contacts with a diameter of 1 mm were thermally evaporated from a Radak source in an Angstrom Nexdep thermal evaporator. Li granules (Alfa Aesar) were evaporated at a rate of $25\,\mathrm{Å\,s^{-1}}$ with a background pressure of 1×10^{-4} Pa. Following the Li evaporation, 100 nm Cu electrodes were also deposited by thermal evaporation at a rate of $1\,\mathrm{Å\,s^{-1}}$ from Cu pellets (Sigma Aldrich) without breaking the vacuum. For the Li/Li symmetric cells, instead of the Pt-coated Si substrates, a sapphire single-crystal substrate (MSE Supplies) was coated with 5 µm Li by thermal evaporation. Sample handling and storage were done in an Ar-filled glovebox line (Inert Corp.) with O_2 and moisture levels below 0.1 ppm. The Orion sputtering system and Angstrom Nexdep evaporation system employed are also connected to the glovebox line, so no exposure to air occurred at any stage of the sample preparation.

1.3 Thin-film solid-state battery

$LiCoO_2$ (LCO) with a thickness of 320 nm was deposited at room temperature by RF magnetron sputtering on a Pt-coated sapphire substrate. A $LiCoO_2$ target from Toshima Manufacturing Co. was sputtered with a power of $5.90\,\mathrm{W\,cm^{-2}}$ and a voltage bias of 70 V applied to the substrate, at a pressure of 3 Pa and employing a gas flow of 24 sccm Ar and 1 sccm O_2. Films were post-annealed at 700 °C for 1 h in a tube furnace (Carbolite Gero GmbH & Co.) at atmospheric pressure with an O_2 flow. The cathode film was coated with 10 nm

$LiNbO_3$ by reactive co-sputtering of a Nb target (Plasmaterials Inc.) and a Li_2O target (Toshima Manufacturing Co.) in an Orion sputtering system with a power of $2.50\,W\,cm^{-2}$ and $5\,W\,cm^{-2}$, respectively, a gas flow of 22.5 sccm Ar and 2.5 sccm O_2, and a chamber pressure of 0.20 Pa. More details on the fabrication and properties of the LCO thin film cathodes can be found in the work by Filippin et al.[S2] On top of the LCO cathode film, an aLLZO electrolyte film with a thickness of 70 nm was deposited as described above. The cells were completed with a 2 µm Li metal anode film deposited by thermal evaporation.

1.4 Through-plane and in-plane aLLZO-coated ceramic LLZO pellets

Commercially-available $Li_{6.25}Ga_{0.25}La_3Zr_2O_{12}$ ceramic pellets (Toshima Manufacturing Co.) with dimensions of 10 mm×10 mm×0.50 mm were used for the Li stripping-plating measurements. To remove surface carbonates and other contaminants, the pellets were heat treated between sacrificial LLZO chunks at 400 °C for 3 h in a tube furnace with O_2 flow. For the through-plane measurements, both sides of the pellet were coated with 10 nm aLLZO following the procedure previously described. For the in-plane measurement, half of the pellet was coated with 10 nm aLLZO and the other half was left uncoated. Lithium metal was deposited on the samples by thermal evaporation as previously described for the Li/Li symmetric cells. For the through-plane samples, a shadow mask with a diameter of 5 mm was used to define the electrode area on both sides of the pellet. For the in-plane configuration, a shadow mask with 1 mm × 2 mm openings spaced at different distances between each other was employed to define the dimensions of the in-plane Li-Cu contacts. The sample were heated to 150 °C for a few minutes to improve the contact between the Li contacts and the LLZO. The through-plane samples were sandwiched between two Cu-coated metallic spacers and contacted using an alligator clamp. The in-plane sample was contacted using tungsten microprobes.

2 Characterization

2.1 Scanning electron microscopy (SEM) imaging

Cleaved cross-sections (Figure 1.b in main text) were imaged with a Hitachi S-4800 field emission gun SEM using an acceleration voltage of 10 kV. Focused-ion-beam (FIB) cuts (Figure 4.a in main text) were performed and imaged in a FEI Helios NanoLab 660 Dual Beam SEM and FIB system. The FIBing process was done with a Ga^+-ion beam at an acceleration voltage of 30 kV with a polishing step at 2 kV. SEM imaging was done with an acceleration voltage of 2 kV.

2.2 Focused-ion-beam time-of-flight secondary-ion-mass spectrometry (FIB-ToF-SIMS)

The chemical structure of the aLLZO film was characterized using time-of-flight secondary ion mass spectrometry (TOF-SIMS)[S3,S4] allowing both, light and heavy, element distribution to be represented in 3D with high spatial resolution and high mass resolution. In this study, a novel method[S5–S7] of combing a HV-compatible high resolution TOF[S8,S9] (H-TOF) from TOFWERK (Thun, Switzerland) with an in situ gas injection system (GIS)[S10] incorporated within a focused ion beam/scanning electron microscope (FIB/SEM) dual-beam instrument from Tescan (Brno, Czech Republic) was used. This technique has been recently reported to provide a significant enhancement of generating secondary ions (up to two orders of magnitude, depending on a material)[S5,S7], resulting in higher signal-to-noise ratio and, therefore increased spatial resolution. Furthermore, a simultaneous co-injection of fluorine gas during a TOF-SIMS measurement shows potential for separating mass interference[S6] (which under standard vacuum conditions constitutes one of the main drawbacks of this technique). Finally, the initial studies seem to indicate that fluorine can have capability of altering the polarity of generated secondary ions during FIB sputtering. This feature, allowing the complete sample's chemical structure to be provided from

a single volume (i.e. without any supplementary gas, two separate measurements have to be conducted to show the distribution of positively and negatively ionizing elements; since TOF-SIMS is a destructive technique, the data has to be acquired from different volumes then), was particularly important in the case of the sample investigated in this work as it enabled to detect elements such as Li (which ionizes positively) and Pt and Au (which dominantly ionizes negatively) in the same measurement. The sample surface was bombarded with a continuous monoisotopic $^{69}Ga^+$ primary ion beam, which was used as both, a sputtering and analysis beam. The 20 kV beam energy was applied to ensure high lateral resolution whilst maintaining sufficient depth resolution. The 4D data set, i.e. a 3D (x, y and z) array with an associated mass spectrum for each data point, was recorded at approx. 110±1 pA ion current and 32 µs dwell time from a 10 µm×10 µm area with 512×512 pixels and 2x2 binning. Figure S1.a shows a secondary electron image of the sputtered crater, with sharp edges and a smooth bottom that indicate no FIB-induced roughness. A XeF_2 precursor was used as a source of fluorine. TOF-SIMS Explorer 1.12.2.0 from TOFWERK (Thun, Switzerland) was used for data collection and analysis. Mass spectra were mass calibrated using the secondary ion signals of the main sample elements ($^7Li^+$, $^{24}Mg^+$, $^{90}Zr^+$, $^{195}Pt^+$ and $^{197}Au^+$), the substrate ($^{28}Si^+$) and the primary ion beam ($^{69}Ga^+$). 3D elemental tomography plots were created using the the Mayavi's *mlab* module for Python.

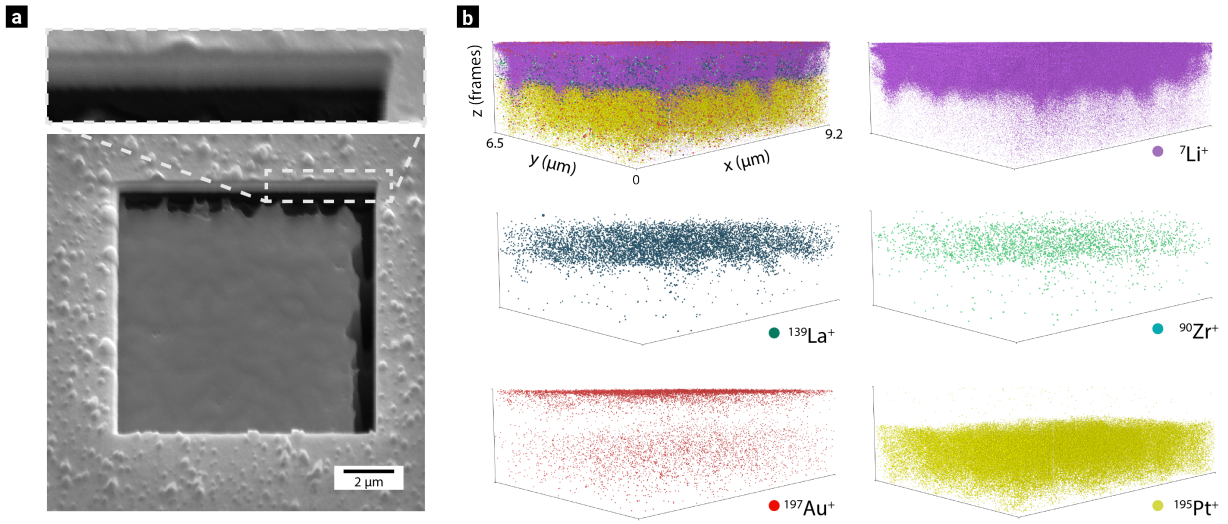

Figure S1: (a) Secondary electron image of the crater after the FIB-ToF-SIMS measurement. Zoomed-in region shows the cross-section of the films. (b) 3D reconstruction of the sample chemical structure obtained from the ToF-SIMS. The signal distribution of the indivitual positively-ionized $^{7}Li^{+}$, $^{139}La^{+}$, $^{90}Zr^{+}$, $^{197}Au^{+}$, and $^{195}Pt^{+}$ isotopes is presented. Upper left plot shows an overlay of all signals.

Standard ToF-SIMS depth profiling was performed with a ToF.SIMS 5 system from IONTOF. For sputtering, a Cs^{+}-ion gun was employed with an acceleration voltage of 2 kV on an area of 300 × 300 µm^2. The primary ion source used for analyzing was Bi^{+} ions with an acceleration voltage of 25 kV. The negative-charged ions extracted from a 100 × 100 µm^2 area within the sputtering crater were used for the analysis. A floodgun was used to avoid surface charging. Figure S2 shows the ToF-SIMS depth profile of extracted negative ions of the oxide compounds composing the aLLZO film (ZrO^{-}, LaO^{-}, and LiO^{-}) and the metal electrodes (Au^{-} and Pt^{-}). In this case, since the measurement was performed in the negative mode without a GIS system, the oxides of Li, La and Zr had to be analyzed instead of the individual isotopes because these elements tend to ionize positively.

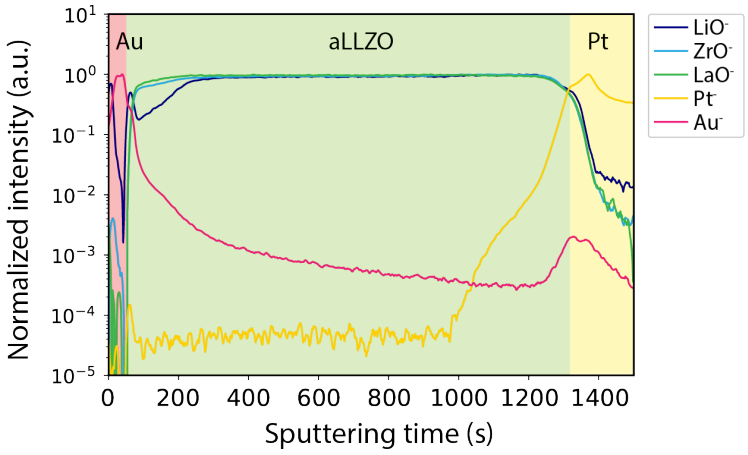

Figure S2: ToF-SIMS depth profile of the negative ions of the main compounds making up the aLLZO electrolyte film (ZrO^-, LaO^-, and LiO^-), the Au top electrode (Au^-) and the Pt back electrode (Pt^-). Three regions are distinguishable: the upper Au contact, the aLLZO film and the Pt back contact.

2.3 X-ray diffractometry (XRD)

XRD diffractograms were acquired in a Bruker D8 Discover XRD system in a grazing-incidence mode with Cu $K_{\alpha 1}$ radiation at an incident angle $\omega = 2°$ and measuring in the range $2\theta = 10°$–$60°$.

2.4 Raman spectroscopy

Raman spectroscopic characterization was performed on a WITec Alpha 300R microscope (300 mm focal length, 600 g/mm grating) equipped with a thermoelectrically cooled EMCCD-Detector. Acquisition parameters for excitation at $\lambda = 532$ nm were optimized for both amorphous and crystallized samples individually to avoid laser-induced changes (40 mW, 25 s integration time and 20 mW, 1 s integration time, respectively. Objective NA = 0.55). Spectra displayed in Figure 1.e are averages of 25(400) spectra acquired over an area of 100 µm (200 µm) for the amorphous (crystallized) sample. Signatures of cosmic rays and a linear background were removed and scaling is indicated in the panel.

2.5 Fourier-transform infrared (FT-IR) spectroscopy

FTIR measurements were conducted with a BRUKER single reflection attenuated total reflection (ATR) unit (diamond ATR crystal) incorporated in a BRUKER Tensor 27 spectrometer in the wavenumber range of 340-4000 cm^{-1}.

2.6 Impedance spectroscopy and current transient measurements

Electrical characterization of the aLLZO films was performed through plane with Pt as back electrode and Au as top electrode using a Paios measurement system (Fluxim AG). Electrochemical impedance spectrocopy (EIS) spectra were recorded between 100 mHz and 10 MHz with an a.c amplitude below 70 mV. Measurements were performed in an Ar filled glovebox at temperatures ranging from room temperature to 200 °C. The temperature was regulated using a Linkam LTSE-420-P heating stage integrated with the measurement system. The temperature on the sample's surface was logged using a PT100 temperature sensor.

The ionic conductivity was extracted from the EIS measurements by fitting the imaginary part of the modulus. Figure S3.a-c shows representative examples of the imaginary modulus for different LLZO:Li_2O mass fractions. The dots indicate the maximum of the imaginary modulus spectra used to calculate ionic conductivity and activation energy from the Arrhenius plot (Figure S3.d).

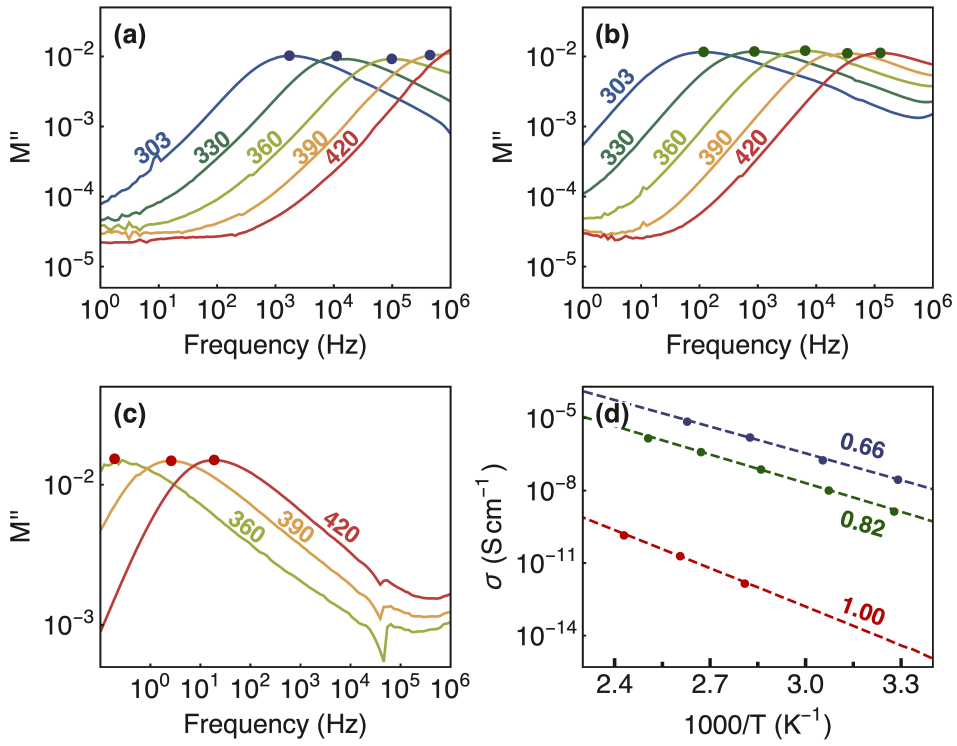

Figure S3: Imaginary part of the modulus of aLLZO samples with LLZO:Li_2O mass fractions of (a) 0.66 (b) 0.82, and (c) 1.00 measured by EIS. (d) Arrhenius plot of the time constants obtained from the imaginary modulus spectra used to calculate activation energies and the ionic conductivities.

To quantify the density of mobile ions, we pre-bias the samples at a positive voltage bias for 1 hour and then measure the current transient after applying a negative voltage bias of same amplitude as the positive one. The current transient is hence representative to the migration of mobile ions from the Au/aLLZO to the Pt/aLLZO interface. Measured current transients for different voltage biases are shown in Figure S4.a-b for two different LLZO:Li_2O mass fractions. After subtracting the background current, the extracted charge is calculated by integration over the measured current transient (Figure S4.c). The ion density n is then calculated from the extracted charge ΔC with $\Delta C = qnd$, where q is the elementary charge and d is the thickness of the aLLZO layer. Figure S4.d shows the obtained mobile ion densities at different voltage biases. At biases higher than 1.20 V the curve begins to flatten, indicating that most of the mobile ions present in the aLLZO layer are being measured.

Here, we use a bias of 2 V for the quantification of the density of mobile ions. However, since larger biases degrade the device, larger densities cannot be excluded.

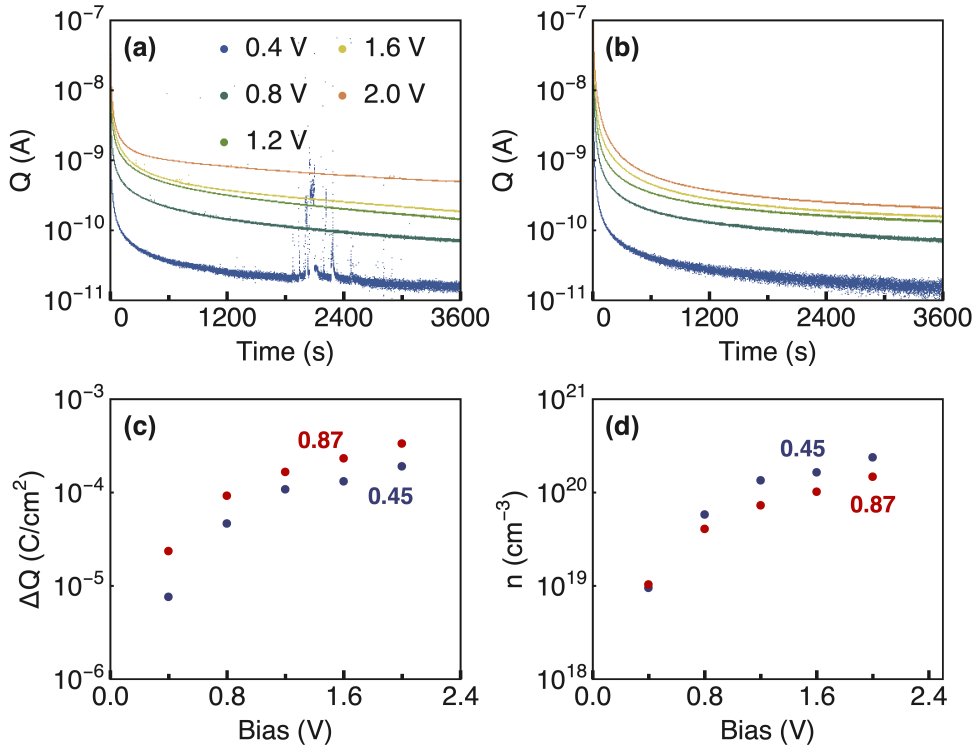

Figure S4: Current transient measurements of aLLZO samples with LLZO:Li_2O mass fractions of (a) 0.45 and (b) 0.87 measured after switching the voltage from a positive to a negative bias. (c) Extracted charge and (d) calculated ion density as a function of voltage bias obtained from the current transients shown in (a-b).

To quantify the electronic conductivity, we measure the steady-state current 1 hour after applying both a positive and a negative bias of 1.2 V. This is shown in Figure S5.a-b as an example, with the obtained electronic conductivities summarized in Figure S5.c. In order to cancel out the effect of the internal electric field due to the different metals used as contacts and possible interfacial effects, we take the mean over both values. The mean values are then used to quantify the activation energies and electronic conductivities, as shown in Figure S4.d. For all the samples with different LLZO:Li_2O mass fractions we obtain an activation energy of 0.35 $\pm$ 0.9 eV and an electronic conductivity of (2.2 $\pm$ 1.4) 10^{-14} S cm^{-1}, which remains fairly constant for the different mass fractions.

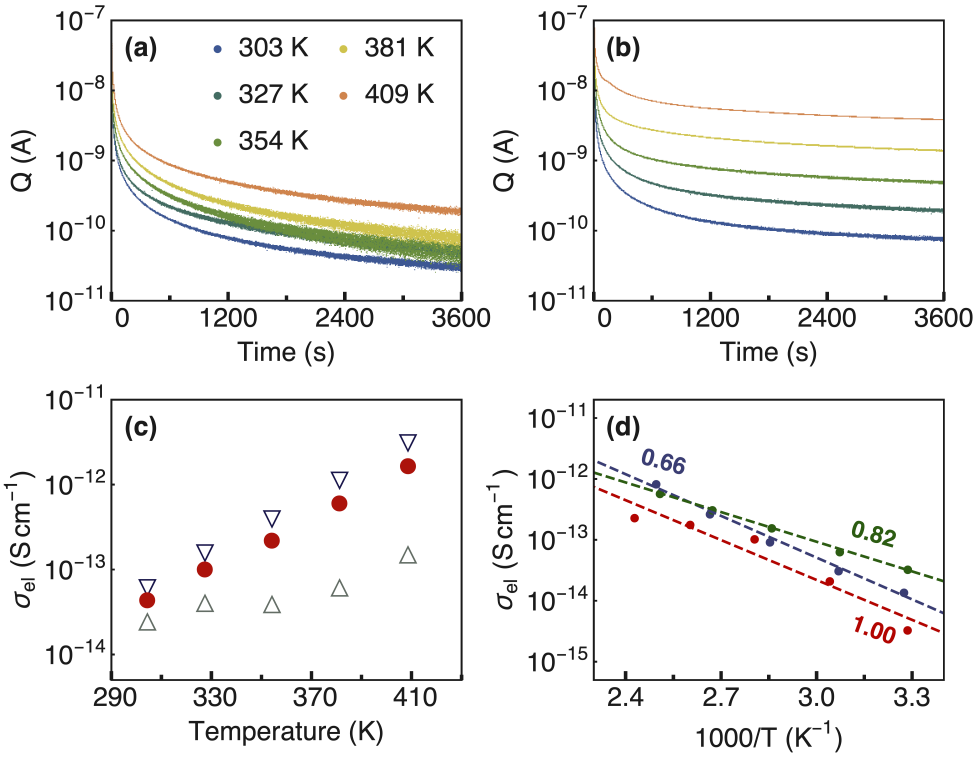

Figure S5: Current transient measurements of an aLLZO sample with a LLZO:Li_2O mass fraction of 0.66 after applying a voltage bias of (a) 1.20 V and (b) −1.20 V. (c) Obtained electronic conductivities of the current transients shown in (a-b). The upright and inverted triangle show the conductivities for applying a positive or negative voltage bias and the circles show the mean of the two values. (d) Arrhenius plot for three different LLZO:Li_2O mass fractions.

2.7 Galvanostatic and potentiostatic cycling of Pt/Li half-cells and symmetric Li/Li cells

To determine the electrochemical stability of the aLLZO electrolyte, the films were measured in galvanostatic and potentiostatic mode in a Pt/Li half-cell. To determine the stability at high potentials, a cyclic voltammetry (CV) measurement was performed between 1 V and 5 V vs. Li/Li^+ at a rate of 2 mV s^{-1} (see Figure S6).

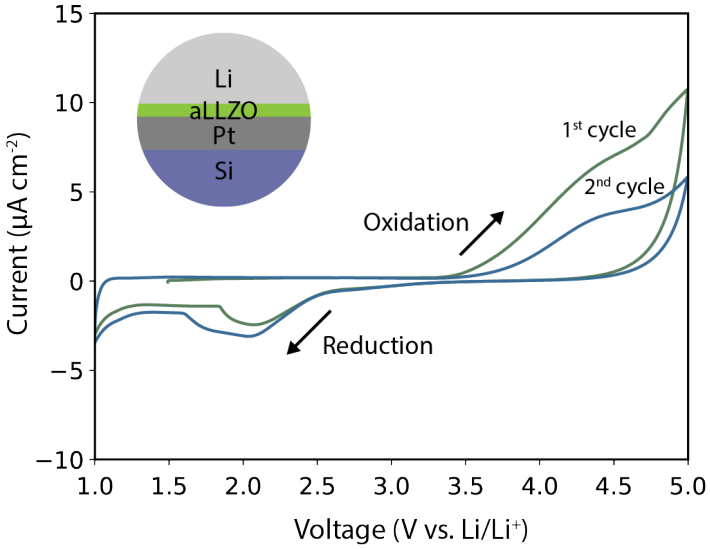

Figure S6: Cyclic voltammetry scans between 1 and 5 V vs. Li/Li^+ of an aLLZO film in a Pt/Li half-cell. Measured with a scan rate of $2\,mV\,s^{-1}$.

To assess the stability versus metallic Li, the half-cell was galvanostatically cycled with a current of $1.25\,\mu A\,cm^{-2}$ around 0 V vs. Li/Li^+ in steps of 1 h. EIS was measured after each step. The resistance of the aLLZO films to Li dendrite penetration was investigated by galvanostatically platting-stripping Li in a symmetric Li/Li cell. The symmetric cells were cycled at increasing current densities, from $0.20\,mA\,cm^{-2}$ up to $3.20\,mA\,cm^{-2}$ for 5 plating-stripping cycles at each current density value. The transferred capacity was limited to $0.10\,mA\,h\,cm^{-2}$, equivalent to a Li thickness of 250 nm.

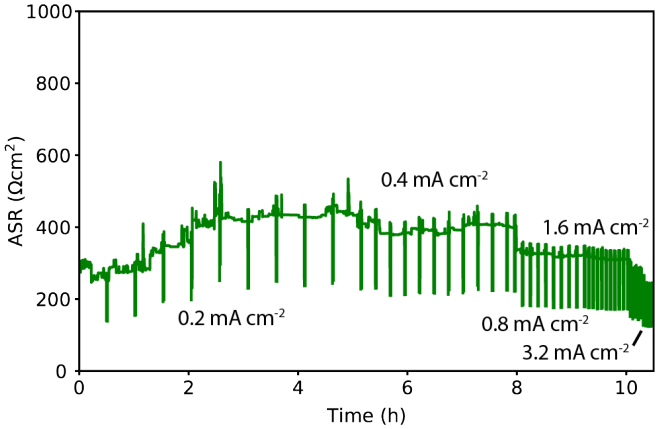

Figure S7: Area specific resistance (ASR) of the symmetric Li/aLLZO/Li cell during Li plating-stripping at different current densities.

2.8 Galvanostatic cycling of thin-film batteries

Charge-discharge curves of the full thin-film battery with aLLZO as electrolyte were recorded in galvanostatic mode within a potential range of 3 V to 4.25 V vs. Li/Li^+. The cells were tested with charge-discharge current densities ranging from 22 µA cm^{-2} (1C) to 0.22 mA cm^{-2} (10C). Long-term cycling was performed at 0.22 mA cm^{-2} for 500 cycles (about 100 h). The oscillations in the discharge capacities are due to temperature variations inside the glovebox between day and night.

2.9 Through-plane Li plating-stripping of Li/crystalline LLZO/Li symmetric cells

Through-plane Li plating-stripping was performed on an aLLZO-coated LLZO pellet and an uncoated pellet as reference. Prior to the plating-stripping process, EIS was measured at room temperature with an amplitude of 10 mV and a frequency range of 1 MHz to 1 Hz. The cells were galvanostatically cycled with symmetric current densities ranging from 5 µA cm^{-2} up to 5.10 mA cm^{-2} in steps of 30 min. The measurements were carried out at room temperature and without external pressure, apart from that of the alligator clamp used

to contact the cell.

2.10 In-plane Li plating-stripping with in-operando microscopy

In-plane Li plating-stripping was performed on the aLLZO-coated and uncoated sides of the ceramic LLZO pellet using the Li metal contacts with a spacing of 0.50 mm. Platting-stripping of Li was performed at current densities ranging from 50 µA cm^{-2} to 3.20 mA cm^{-2} for a total charge transfer of 25 µA h cm^{-2}, with 15 min rest steps in between. During the Li platting-stripping process, a Dino-Lite AM73115MZT digital microscope was used to monitor the surface of the LLZO pellet.

References

(S1) Sastre, J.; Priebe, A.; Döbeli, M.; Michler, J.; Tiwari, A. N.; Romanyuk, Y. E. Lithium Garnet $Li_7La_3Zr_2O_{12}$ Electrolyte for All-Solid-State Batteries: Closing the Gap between Bulk and Thin Film Li-Ion Conductivities. *Adv. Mater. Interfaces* **2020**, 2000425.

(S2) Filippin, A. N.; Lin, T.-Y.; Rawlence, M.; Zünd, T.; Kravchyk, K.; Sastre-Pellicer, J.; Haass, S. G.; Wäckerlin, A.; Kovalenko, M. V.; Buecheler, S. Ni–Al–Cr Superalloy as High Temperature Cathode Current Collector for Advanced Thin Film Li Batteries. *RSC Adv.* **2018**, *8*, 20304–20313.

(S3) Benninghoven, A.; Rudenauer, F. G.; Werner, H. W. Secondary Ion Mass Spectrometry: Basic Concepts, Instrumental Aspects, Applications and Trends. **1987**,

(S4) van der Heide, P. *Secondary Ion Mass Spectrometry: An Introduction to Principles and Practices*; John Wiley & Sons, 2014.

(S5) Priebe, A.; Utke, I.; Pethö, L.; Michler, J. Application of a Gas-Injection System during the FIB-TOF-SIMS Analysis—Influence of Water Vapor and Fluorine Gas on Secondary Ion Signals and Sputtering Rates. *Anal. Chem.* **2019**, *91*, 11712–11722.

(S6) Priebe, A.; Pethö, L.; Michler, J. Fluorine Gas Coinjection as a Solution for Enhancing Spatial Resolution of Time-of-Flight Secondary Ion Mass Spectrometry and Separating Mass Interference. *Anal. Chem.* **2020**, *92*, 2121–2129.

(S7) Priebe, A.; Xie, T.; Pethö, L.; Michler, J. Potential of Gas-Assisted Time-of-Flight Secondary Ion Mass Spectrometry for Improving the Elemental Characterization of Complex Metal-Based Systems. *J. Anal. At. Spectrom.* **2020**,

(S8) Whitby, J. A.; Östlund, F.; Horvath, P.; Gabureac, M.; Riesterer, J. L.; Utke, I.; Hohl, M.; Sedláček, L.; Jiruše, J.; Friedli, V.; Bechelany, M.; Michler, J. High Spatial Resolution Time-of-Flight Secondary Ion Mass Spectrometry for the Masses: A Novel Orthogonal ToF FIB-SIMS Instrument with *In Situ* AFM. *Adv. Mater. Sci. Eng.* **2012**, *2012*, 1–13.

(S9) Alberts, D.; von Werra, L.; Oestlund, F.; Rohner, U.; Hohl, M.; Michler, J.; Whitby, J. A. Design and Performance of Two Orthogonal Extraction Time-of-Flight Secondary Ion Mass Spectrometers for Focused Ion Beam Instruments. *Instrum. Sci. Technol.* **2014**, *42*, 432–445.

(S10) Wang, Z. M. *FIB Nanostructures*; Springer Science & Business Media, 2014.